ROYAL SOCIETY
OF CHEMISTRY

Check for updates

Design principles of biphenylene-supported dual-atom catalysts for efficient and selective nitrate reduction to ammonia

Kiruthika Pandiyan [ID] and Hsin-Tsung Chen [ID] *

The electrochemical nitrate reduction reaction (NO₃RR) offers a sustainable approach for converting nitrate pollutants into valuable ammonia under ambient conditions. Herein, we employ density functional theory (DFT) to systematically investigate the catalytic potential of homonuclear transition metal dual-atom catalysts (DACs) anchored on biphenylene (TM_2@BPN) for NO₃RR. Among 28 candidates, five DACs: Mo_2@BPN, Ru_2@BPN, Rh_2@BPN, Os_2@BPN, and Ir_2@BPN, exhibit low limiting potentials (−0.40 to −0.16 V) and exceptional ammonia selectivity. Rh_2@BPN, in particular, achieves a theoretical faradaic efficiency of 100%, effectively suppressing competing hydrogen evolution. Electronic analyses reveal that dual-site π-donation/π*-back-donation interactions, d-band center tuning, and charge redistribution collectively enhance NO_3^- activation compared to single-atom analogues. Importantly, descriptor-based volcano plots (ΔG_{*NO_3}, ε_d, and ψ) establish generalizable design rules that correlate electronic structure with catalytic trends, enabling predictive DAC screening beyond exhaustive pathway calculations. *Ab initio* molecular dynamics simulations further confirm the thermal stability of the most active DACs. This work introduces biphenylene as a robust support for stabilizing DACs, establishes structure–property–performance correlations, and provides transferable mechanistic and descriptor-based insights for the rational design of next-generation catalysts for selective multi-electron electrochemical transformations such as nitrate-to-ammonia conversion.

1. Introduction

Nitrate contamination has emerged as a global environmental concern due to the excessive use of fertilizers, industrial emissions, and wastewater discharge. The accumulation of nitrate in aquatic systems not only disrupts ecosystems but also poses severe health risks upon conversion to toxic nitrites in the human body.[1–5] Traditional remediation strategies—chemical, physical, or biological—often suffer from high cost, energy intensity, or operational complexity.[6,7] In contrast, the electrochemical nitrate reduction reaction (NO₃RR) offers a sustainable route to both detoxify nitrate and synthesize ammonia (NH₃), a valuable chemical feedstock and potential hydrogen carrier.[8–12] While the Haber–Bosch process remains the industrial standard for ammonia synthesis, it is highly energy-intensive and carbon-emissive. Direct electrochemical ammonia production *via* the nitrogen reduction reaction (NRR) is appealing but limited by the inertness of N₂ and its low solubility.[13–15] In comparison, NO₃RR is more kinetically favorable due to the lower bond dissociation energy of the N–O bond

and the higher solubility of nitrate in aqueous media, making it a promising alternative for green ammonia synthesis.[16] However, NO₃RR is a complex eight-electron, nine-proton transfer process with multiple intermediates and competing side reactions such as hydrogen evolution.[17–19] Achieving high activity and selectivity requires the development of advanced catalysts with well-tuned binding energies. Single-atom catalysts (SACs) have drawn significant interest due to their maximal atom utilization and high activity, but their isolated active sites often struggle with multistep reactions due to linear scaling limitations.[20–23]

Dual-atom catalysts (DACs), comprising two adjacent metal atoms, have recently emerged as a promising class of materials that combine the advantages of SACs with synergistic effects. These dual sites enable independent optimization of multiple reaction steps, making DACs particularly attractive for complex processes like NO₃RR.[24–28] For example, the Cu₂ embedded on n-doped graphene was experimentally verified and exhibited good activity for NO₃RR with 97.4% faradaic efficiency.[29] Fe/Cu diatomic catalysts on nitrogen-doped graphene achieving faradaic efficiencies up to 92.5% at −0.3 V *vs.* RHE demonstrate strong potential, yet they often rely on heterogeneous dual-atom sites and systematic prediction and design of homonuclear DACs has been less explored.[30] Additionally, high-throughput computational screening of M₁M₂@g-CN DACs (eg FeMo@g-

Department of Chemistry, Research Center for Semiconductor Materials and Advanced Optics, and R&D Center for Membrane Technology, Chung Yuan Christian University, Chungli District, Taoyuan City 320314, Taiwan. E-mail: htchen@cycu.edu.tw; Tel: +886-3-265-3324

CN, CrMo@g-CN) has identified promising heterogeneous dual-metal combinations, but descriptors correlating electronic structure to performance are still diverse.[31] Moreover, reviews of NO_3RR underscore that mechanical understanding, especially linking the electronic structure of active dual metal sites, to ammonia selectivity, remains underdeveloped.[32] Despite recent progress, rational screening of DACs for NO_3RR remains limited, and suitable supports that can stabilize and electronically engage dual-metal centers are critically needed. In particular, the potential of homonuclear DACs for NO_3RR remains largely unexplored, how the electronic structure of homonuclear DACs influences the activity and selectivity towards ammonia formation, and reliable electronic descriptors for predicting their catalytic behavior are still lacking.

Herein, we explore biphenylene (BPN)—a recently synthesized sp^2-hybridized carbon allotrope featuring four-, six-, and eight-membered rings—as a novel support for homonuclear transition metal DACs. Unlike graphene and other 2D carbon materials the intrinsic ring topology provides a porous lattice with a large number of low-coordination sites that can efficiently stabilize metal atoms. In specific cases, BPN outperforms graphene in catalytic performance due to its higher σ-center position (-7.49 eV vs. -8.09 eV), which allows for greater interaction with reaction intermediates. BPN offers high thermal stability with high thermal conductivity and electrical stability and unique electronic properties including metallic behavior with a tilted Dirac cone above the Fermi level and strong in-plane anisotropy conducive to electrocatalysis.[33–37] BPN is a promising catalyst for various reactions, including HER,[38] OER,[39] CO_2RR,[40] and NRR.[41] In addition, BPN can anchor transition-metal atoms without needing engineered defects or dopant heteroatoms, leading to highly active single-atom Pd@Bip catalysts with very low overpotentials for HER (~0.05 V) and OER (~0.50 V), outperforming many conventional catalysts.[42] Given the unique advantages of BPN, it is desirable to investigate the potential of BPN for NO_3RR and its underlying catalytic mechanism, which has not been reported until now.

Using density functional theory (DFT), we systematically investigate 28 TM_2@BPN catalysts for NO_3RR, evaluating their activity, selectivity, electronic structure, and thermal stability. After assessing 28 candidates of TM_2@BPN, 21 homonuclear DACs that exhibit thermodynamic stability were selected for further investigation. Our screening identifies five promising DACs, Mo_2@BPN, Ru_2@BPN, Rh_2@BPN, Os_2@BPN, and Ir_2@BPN that exhibit low limiting potentials and excellent selectivity toward NH_3. In particular, Rh_2@BPN demonstrates a theoretical faradaic efficiency of 100%. Electronic structure analysis, descriptor-based volcano plots, and ab initio molecular dynamics simulations reveal structure–property–performance relationships that provide fundamental insight and design principles for next-generation NO_3RR catalysts.

2. Computational details

All spin-polarized density functional theory (DFT) computations were performed using the Vienna ab initio simulation package (VASP).[43] The projected augmented wave (PAW)[44] approach was used to characterize ion–electron interactions. The generalized gradient approximation in the form of the Perdew–Burke–Ernzerhof (PBE)[45] functional was used to treat the exchange correlation energy. The DFT-D3 approach is used to correct van der Waals interactions.[46] An energy cutoff of 500 eV was adopted for the plane-wave basis. To prevent interactions between periodic pictures, a 15 Å vacuum space was employed perpendicular to the 2D layer. The convergence criteria for force and total energy during the structural optimization were 0.02 eV $Å^{-1}$ and 10^{-5} eV, respectively. For structural optimizations, the Monkhorst-Pack[47] approach was used to sample the Brillouin zone with $3 \times 3 \times 1$ k-points, while electronic property computations employed denser k-points of $6 \times 6 \times 1$. Ab initio molecular dynamic (AIMD)[48] simulation is used to determine the catalysts' thermal stability, with a temperature of 500 K and a simulation time of 10 ps. The charge transfer was analyzed using the Bader charge technique.[49] To examine the electron interaction, the projected crystal orbital Hamiltonian populations (pCOHP)[50] were computed. In the NO_3RR, the adsorption energies of every potential intermediate are described as,

$$E_{ads} = E_{total} - E_{substrate} - E_{adsorbate} \quad (1)$$

where E_{total}, $E_{substrate}$, and $E_{adsorbate}$ are the total energies of the adsorbed intermediate on TM_2@BPN, the TM_2@BPN and the isolated adsorbate, respectively. The computational hydrogen electrode (CHE)[51] model was used to determine the Gibbs free energy (ΔG) changes for stepwise hydrogenation and electron transfer ($H^+ + e^-$) during the NO_3RR process. The ΔG for each intermediate step in NO_3RR is defined as follows:

$$\Delta G = \Delta E + \Delta E_{ZPE} - T\Delta S + \Delta G_U + \Delta G_{pH} \quad (2)$$

where ΔE is the total energy change obtained from the DFT calculation, ΔE_{ZPE} and $T\Delta S$ are the zero-point energy and the change in entropy respectively, and T is temperature at 298.15 K. Additionally, the entropy of the gaseous molecules was obtained from the National Institute of Standards and Technology (NIST) database (Table S1), while the ZPE and entropy of the intermediates were computed using the harmonic approximation based on the normal-mode vibrational frequencies.

ΔG_U is the applied potential with 0 V in this study, and ΔG_{pH} is considered as the correction free energy of H^+, which can be calculated using the equation that follows:

$$\Delta G_{pH} = 2.303 \times k_B T \times pH \quad (3)$$

where k_B is the Boltzmann constant and pH is set to zero to represent an acidic environment. The limiting potential (U_L) is the lowest potential in the NO_3RR process, used to evaluate the catalytic activity of electrocatalytic reactions. It can be defined as follows:

$$U_L = -\Delta G_{max}/e \quad (4)$$

where, ΔG_{max} is the maximum free energy change in the potential-determining step (PDS). In order to avoid calculating the energy of charged NO_3^- directly, we used gaseous HNO_3 as

a reference. The adsorption energy of NO_3^- (ΔG_{*NO_3}) was obtained as follows:

$$\Delta G_{*NO_3} = G_{*NO_3} - G_* - G_{HNO_3 \text{ (g)}} + 1/2 G_{H_2 \text{ (g)}} + \Delta G_{correct} \quad (5)$$

where G_{*NO_3}, G_*, $G_{HNO_3 \text{ (g)}}$ and $G_{H_2 \text{ (g)}}$ are the Gibbs free energy of NO_3^- adsorbed on TM_2@BPN, TM_2@BPN, gaseous HNO_3, and H_2 molecules, respectively. $\Delta G_{correct}$ denotes the correction of adsorption energy and is set to 0.392 eV.[52] The computational details of $\Delta G_{*intermediate}$ and solvent effect are given in SI (Note S1 and S2).

3. Results and discussion

3.1 Structure of BPN and stability of TM_2@BPN

Fig. 1a shows the optimal structure (3 × 3) of biphenylene, a two-dimensional material containing two chemically different carbon sites, namely C_1 and C_2. Our optimized BPN lattice parameters were $a = 4.52$ Å and $b = 3.77$ Å, consistent with prior computational results.[53] BPN is structured with alternating four, six, and eight-membered carbon rings, this arrangement distinguishes it from graphene and other sp^2-carbon networks, resulting in distinct electrical and geometric features. Density functional theory studies have revealed that the non-uniform C–C bonds in biphenylene results in anisotropic electronic characteristics. We calculated the electron localization function (ELF) to acquire additional insights into the electrical structure of the BPN.

As shown in Fig. 1b, the electron localization function of BPN ranges from 0 au (blue) to 1 au (red), where higher values indicate stronger electron localization. The BPN showed discrete regions with values of roughly 0.5 au, indicating delocalized electrical structure. The C–C bond has a maximum value of around 0.9 au, indicating the presence of a strong covalent connection in BPN.

The TM_2@BPN system was designed by anchoring 28 TM dimers (TM = 3d, 4d, 5d) to the BPN surface. As shown in Fig. S1, four potential TM dimer anchoring configurations were

considered: (I) C1–C1 bridging in a six-membered ring, (II) C1–C1 bridging in an eight-membered ring, (III) top C1 site in an eight-membered ring, and (IV) C2–C2 bridging in an eight-membered ring. The stability and relative energy of these TM dimer anchoring configurations have been thoroughly investigated in previous reports.[41] Fig. 2a depicts the most stable anchoring configurations after the structural optimization. Using the most energetically favorable configurations, we investigated the stability of TM_2@BPN by calculating the binding and cohesive energy. To assess the binding strength between the TM dimer and the BPN substrate, the binding energy (E_{bin}) was calculated as follows:

$$E_{bin} = E_{TM2@BPN} - E_{BPN} - 2E_{TM} \quad (6)$$

where E_{BPN} represents the energy of the pure BPN substrate, E_{TM} represents the energy of the isolated metal atoms, and $E_{TM2@BPN}$ represents the total energy of the BPN catalyst. In order to determine the TM atoms' tendency to aggregate on BPN, the cohesive energy (E_{Coh}) was computed as follows:

$$E_{coh} = (E_{bulk} - nE_{TM})/n \quad (7)$$

where E_{bulk} represents the energy of the metal bulk, E_{TM} represents the energy of isolated metal atoms, and n represents the total number of metal atoms in the bulk. Fig. 2b provides the plot of the binding and cohesive energies, and Table S2 summarizes the corresponding values. The binding energies of all the TM_2@BPN are negative, suggesting that the doping of the TM dimer on the BPN substrate is energetically favorable. To ensure the stability of the dual metal system and inhibit diffusion or aggregation, the binding energy should be lower than or comparable with the cohesive energy. Accordingly, we have neglected the metal dimers Cr_2, Cu_2, Zn_2, Ag_2, Cd_2, Au_2, and Hg_2. Table S3 provides the electronic and structural properties of TM_2@BPN, including TM dimer bond length, charge transfer, and d-band center. The distance between the TM dimer varies from 4.09 Å for Y_2 to 1.72 Å for Mo_2. Moreover, a charge transfer of 0.61 to 4.41 e$^-$ from the TM dimers to the BPN
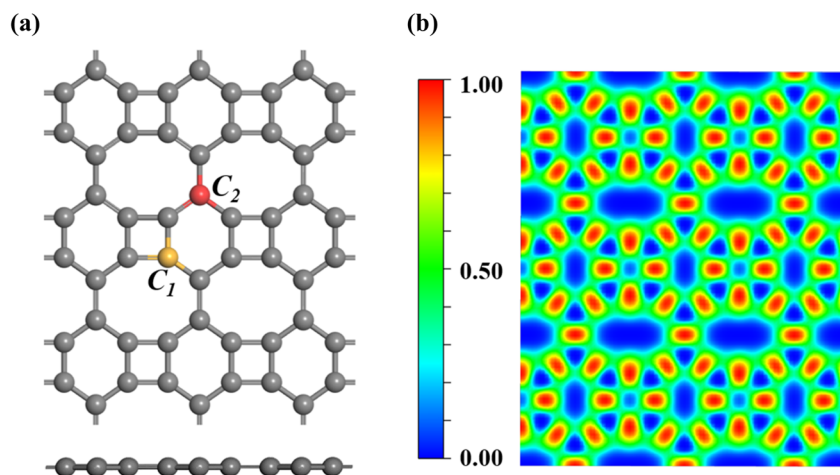

Fig. 1 (a) Optimized structure of BPN substrate, with C_1 and C_2 carbon highlighted. (b) The electron localization function (ELF) of BPN.
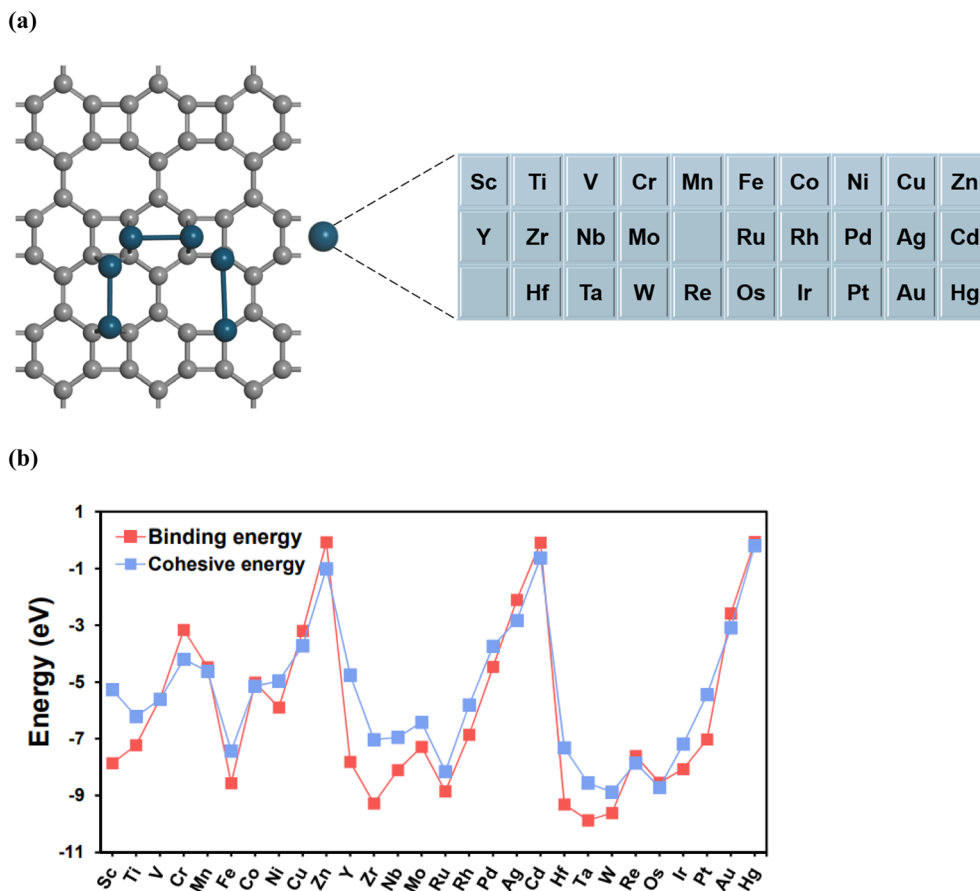
(a)

(b)

Fig. 2 (a) The stable binding configurations of TM$_2$@BPN, with 28 transition metals considered for anchoring on BPN substrate, (b) Binding and cohesive energy comparison plot for TM$_2$@BPN.

substrate induces significant positive charges on the metals, which enhances their interaction with the substrate and contributes to their stabilization. The positive charge on these metal dimers enhances the adsorption of NO$_3$RR intermediates, hence accelerating the process.

3.2 NO$_3^-$ adsorption

The initial phase of the NO$_3$RR process entails the adsorption of nitrate, a decisive factor that determines the overall catalytic reaction. Dual metal sites provide multiple adsorption possibilities for the NO$_3^-$ adsorbate. In this study we have considered three different adsorption configurations in order to determine the most stable NO$_3^-$ adsorption on the catalyst surface. The geometries are based on the number of oxygen atoms bonded to the active sites: monodentate (η^1-O-1) when a single oxygen binds to one metal site; chelating bidentate (η^2-O-1) when two oxygens bind to the same metal site; and bridging bidentate (η^2-O-2) when two oxygens bridge between two metal sites (Fig. S2). As summarized in Table S4, our findings indicate that the NO$_3^-$ prefers to form a bond with the dual metals by adopting a (η^2-O-2) bidentate configuration. The bond length between the metals and oxygen atom is less than 3Å (Table S5), indicating that the bidentate configuration has a strong hold of NO$_3^-$. The presence of H$^+$ ions in the reaction promotes competition between

NO$_3$RR and HER, resulting in low selectivity and faradaic efficiency of the NO$_3$RR catalyst. In this study, we have investigated two approaches for evaluating the catalyst's selectivity: comparing the adsorption free energy of *NO$_3^-$ and *H on the catalyst and comparing the limiting potential of HER and NO$_3$RR. First, we will consider the adsorption free energies. Fig. 3a displays the adsorption free energies of NO$_3^-$ (ΔG_{*NO_3}), and H (ΔG_{*H}), for comparison. The results revealed that ΔG_{*NO_3} values are significantly more negative (ranging from -3.20 eV to -0.91 eV) than ΔG_{*H} (ranging from -1.52 eV to 0.43 eV), and this trend is consistent across all TM$_2$@BPN systems. Thus, the active regions of the TM dimers will predominantly adsorb NO$_3^-$ over H atoms, thereby suppressing the HER. Table S6 summarizes the calculated values of the *H adsorption free energies. The adsorption free energy values of *NO$_3^-$ indicates that the early transition metals display stronger chemisorption as compared to later transition metals. This behavior can be attributed to early transition metals having fewer d electrons, resulting in greater d-orbital availability and consequently, stronger adsorption; in contrast, late transition metals exhibit a reverse trend. Fig. 3b displays the relationship between the charge transfer of the TM dimer and the adsorption free energy of *NO$_3^-$ (ΔG_{*NO_3}), for better comprehension of the *NO$_3^-$ adsorption pattern on TM$_2$@BPN (Table S7). There is a linear
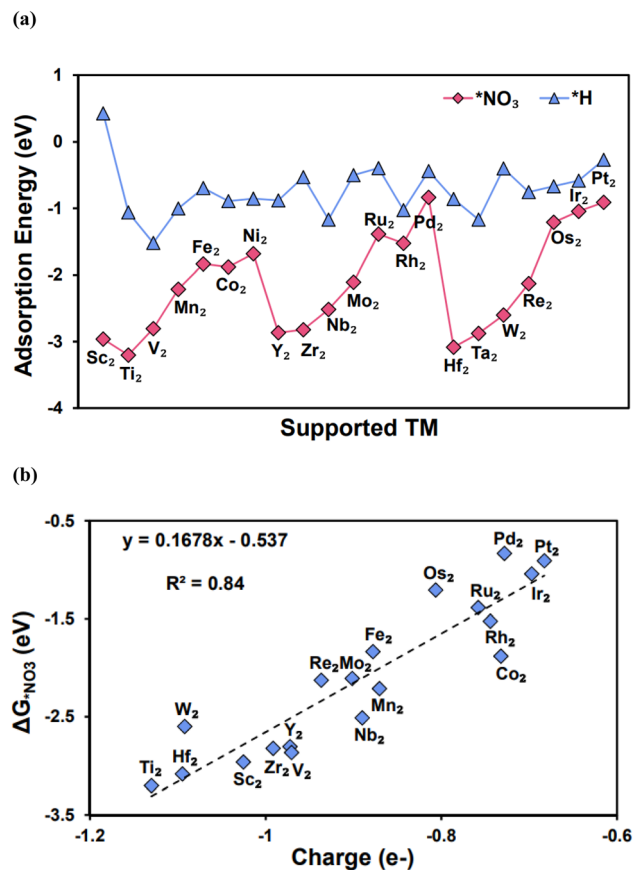
(a)

(b)

Fig. 3   (a) Comparison of adsorption free energies of NO_3^-, and H on TM_2@BPN. (b) The scaling relationship between NO_3^- adsorption free energies and charge transfer of TM dimers.

relationship with a strong correlation coefficient of $R^2 = 0.84$, which confirms that stronger NO_3^- adsorption is attributed to a substantial charge transfer from the TM dimer to the adsorbate. For illustration, Ti_2@BPN has the strongest adsorption strength of -3.20 eV and the maximum charge transfer of 1.13 e$^-$.

3.3   NO$_3$RR mechanism on TM$_2$@BPN

The process of NO_3RR proceeds *via* the transfer of eight electrons and nine protons.[13] The intricacy of the reaction mechanism originates from a complex network of intermediates and byproducts, including NO, NO_2, N_2O and N_2. Additionally, a wide range of intermediate adsorption configurations are possible, resulting in numerous hydrogenation sites for each intermediate. To forecast the most optimal reaction mechanism on TM_2@BPN, the stable intermediate from each step is chosen for the subsequent hydrogenation step. Fig. 4 shows the possible NO_3RR pathways on TM_2@BPN. Nitrate ion adsorption (η^2-O-2) serves as the primary step in the reaction mechanism, the most readily accessible O atom is then protonated, and a N–O bond is broken, forming *OH–*NO$_2$. The subsequent hydrogenation leads to the formation of the *NO$_2$ intermediate. After two hydrogenations, the water molecule is released, generating a crucial intermediate, *NO. In TM_2@BPN, the *NO

adsorption favors both side-on and end-on configurations. Thereby, protonation of *NO leads to the formation of ammonia and an additional water molecule on the substrate.

3.3.1   Limiting potential. The limiting potential (U_L) serves as a critical determinant of catalytic activity since it represents the most energy-intensive step in the reaction. Therefore, we determined the limiting potential of TM_2@BPN to assess the NO_3RR performance. The limitation potentials of TM_2@BPN for NO_3RR to generate NH_3 are summarized in Fig. 5 and Table S8. We set a benchmark limiting potential of (>-0.50 V) on TM_2@BPN for NO_3RR, based on the experimentally reported limiting potentials for graphene and previously published catalysts.[26,29,54] Catalysts meeting this benchmark are expected to demonstrate better catalytic activity. Most of the DACs exhibit best limiting potentials, signifying that NO_3RR can be effectively catalyzed on TM_2@BPN. Rh_2@BPN exhibits the lowest limiting potential of -0.16 V, further five additional DACs, Mo_2@BPN, Ru_2@BPN, Os_2@BPN, Ir_2@BPN and Pt_2@BPN exhibit low limiting potentials, with values of -0.40, -0.36, -0.32, -0.35, and -0.45 V respectively.

Descriptor based catalyst design serves as a more effective and focused approach for electrocatalytic development and screening.[55] The Gibbs free energies of intermediates, which play a critical role in chemical reactions, can function as a primary indicator for predicting the catalytic activity. Therefore, the Gibbs free energy of NO_3^- is chosen as a descriptor, as nitrate is a key intermediate and its adsorption is an essential step. Fig. 6 shows the graph of limiting potential plotted as a function of the Gibbs free energy of NO_3^-. Apparently, there is a distinct volcano shaped relationship between them with Rh_2@BPN precisely situated at the top of the volcano plot. Apart from, Rh_2@BPN additional TM_2@BPN systems (highlighted in purple in Fig. 6) are characterized by low limiting potentials (U_L). We can deduce that, insufficient adsorption of the catalyst results in a potential determining step (PDS) from *NO to *NOH, while intense adsorption results in high energy demanding step from *NH$_2$ to *NH$_3$/*OH to *OH$_2$. This analysis is consistent with the Sabatier principle, which states that the ideal catalytic activity is achieved if the essential intermediates and catalysts bind with moderate intensity. Accordingly, catalysts with moderate adsorption (ΔG_{*NO_3} between -1.5 to 0.9 eV) have high catalytic activity.

We determined the Gibbs free energy profiles for NO_3RR on Rh_2@BPN, Os_2@BPN, and Ir_2@BPN, (Fig. 7a–c) surfaces in order to gain more insight into the reaction mechanism of nitrate reduction to NH_3. The DFT-optimized configurations of intermediates associated with the free energy diagram of Rh_2@BPN, Os_2@BPN and Ir_2@BPN are shown in Fig. S3, the computed zero-point energy and entropy are listed in Table S9–S11, and the Gibbs free energy profiles for the remaining DACs are shown in Fig. S4–S9. It is evident that NO_3^- is strongly chemisorbed on Rh_2@BPN, Os_2@BPN, and Ir_2@BPN *via* two TM–O bonds, with free energy changes of -1.52, -1.21, -1.04 eV respectively. On Rh_2@BPN, the initial proton–electron coupling preferentially attacks the nitrate oxygen interacting with Rh over terminal oxygen. As a result, NO_3 dissociates to form *OH–*NO$_2$ with an energy release of -1.35 eV. A similar
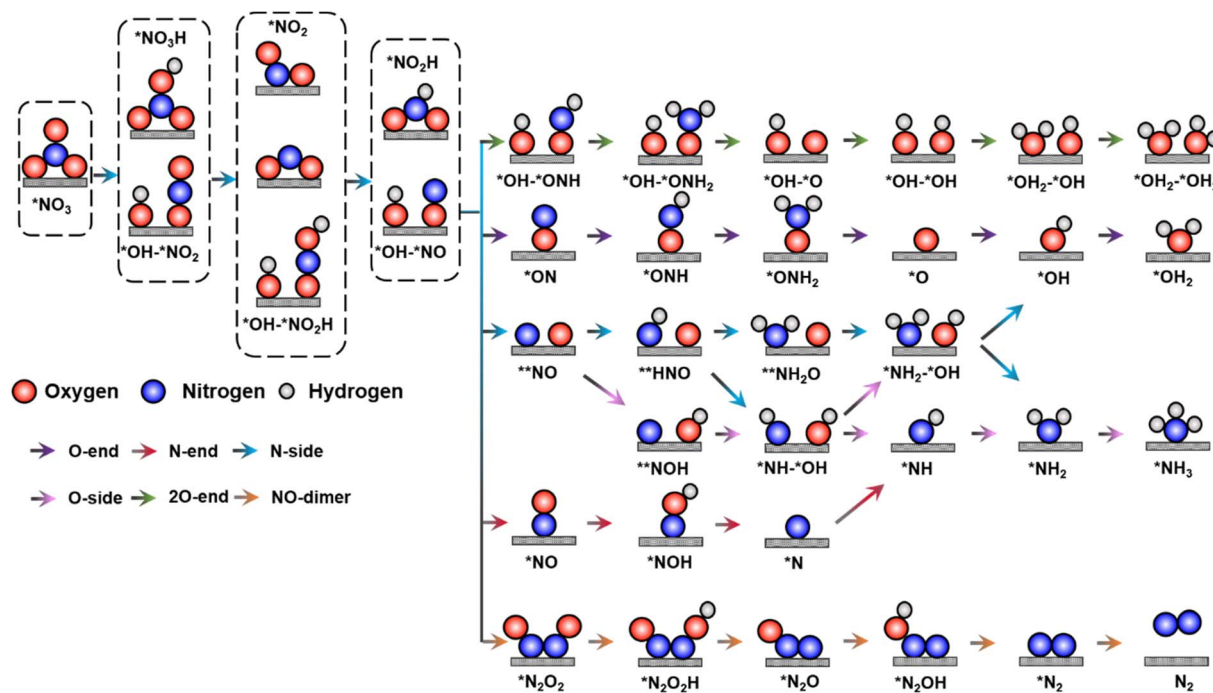
Fig. 4 Detailed reaction pathway for NH_3 production, as well as NO dimer pathway for N_2O, and N_2 production.

trend can be identified on Os_2@BPN and Ir_2@BPN with an exothermic energy change of -2.88 eV, and -2.09 eV respectively. The second hydrogenation step leads to the formation of H_2O, which possesses greater energetic stability than the hydrogenation of the $*OH–*NO_2$ molecule to $*OH–*NO_2H$. This step is exothermic by -1.19 eV for Rh_2@BPN, and leaves the $*NO_2$ on the active site with two Rh–O bonds. Then $*NO_2$ undergoes hydrogenation in the third step, analogous to that of $*NO_3^-$ to form $*OH–*NO$ with an energy release of -1.40 eV. The fourth hydrogenation results in the formation of $*NO$ on the Rh–Rh bridging site, following the release of the second water molecule. Three different bonding modes were assessed for $*NO$ adsorption: $**NO$ (binding via the NO-side), $*ON$

(binding via the O-end), and $*NO$ (binding via the N-end) as shown in Fig. S10. Depending on the $*NO$ configuration (NO-end, NO-side, and ON-end), the following hydrogenation will adopt a different pathway. The computed Gibbs free energy for all the binding modes of $*NO$ is tabulated in Table S12. The findings indicate that $*NO$ and $**NO$ modes are thermodynamically more favorable than $*ON$ mode. On Rh_2@BPN, $*NO$ is more likely to adsorb via side-on mode ($**NO$). The hydrogenation of $**NO$ requires an energy input of 0.16 eV to generate $**HNO$ on the active site. Proceeding with the reactions, steps six to eight are enzymatic protonation of the intermediates ($*NH–*O → *NH–*OH → *NH_2–*OH → *NH_2$), with corresponding energy changes of -0.34, -1.06, and -0.63 eV
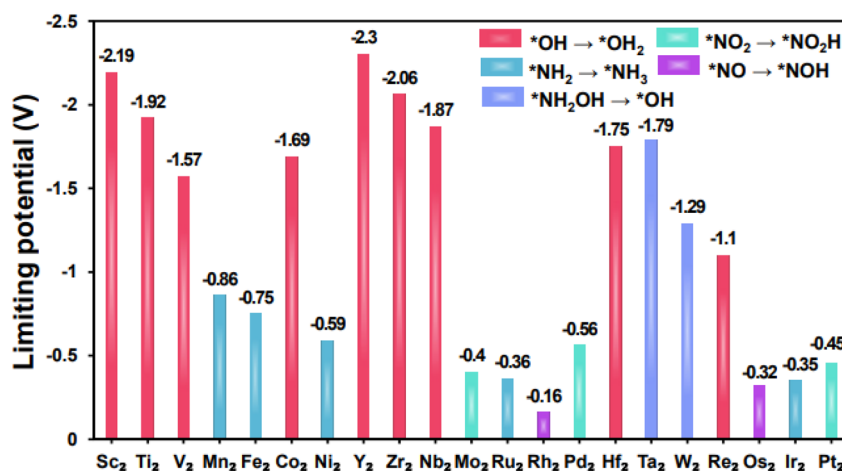

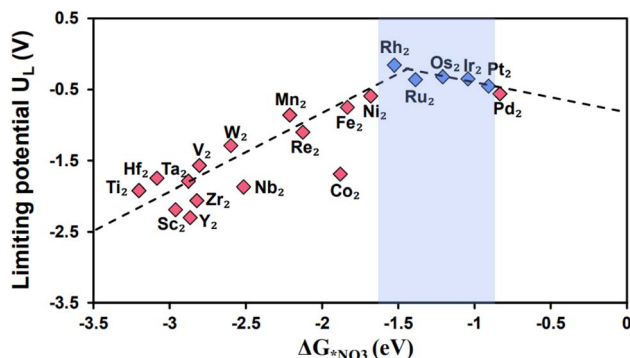**Fig. 5** The computed limiting potential of TM_2@BPN for NO_3RR.

Fig. 6 NO$_3$RR Volcano plot of TM$_2$@BPN with the descriptor of Gibbs free energy NO$_3$ (ΔG_{*NO3}) *vs.* limiting potential (U_L).

respectively, to release the third water molecule and leave *NH$_2$ on the active site. Eventually the *NH$_2$ can be protonated to generate *NH$_3$ with a Gibbs free energy change of 0.04 eV. The potential determining step of NO$_3$RR on Rh$_2$@BPN is the conversion of *NO → *HNO with a low U_L of −0.16 eV.

On Os$_2$@BPN, the hydrogenation of *OH–*NO$_2$ results in the formation of NO$_2$ on the active site with two Os–O bonds, this step involves an endothermic contribution of 0.26 eV. Further hydrogenation results in the formation of *NO. On Os$_2$@BPN *NO adsorption prefers the end on mode (*NO) with an energy release of −0.53 eV. The hydrogenation of *NO requires an energy input of 0.32 eV to generate *NOH on the active site. The ensuing hydrogenations are all exothermic and proceed along the *NOH → *N → *NH → *NH$_2$ → *NH$_3$ pathway. The potential determining step of NO$_3$RR on Os$_2$@BPN is the conversion of *NO → *HNO with a U_L of −0.32 eV. For Ir$_2$@BPN the adsorption configuration of *NO$_3$ and *NO intermediates and reaction steps throughout the entire protonation pathway are consistent with Os$_2$@BPN. During the entire protonation mechanism on Ir$_2$@BPN, the conversion of NH$_2$ → NH$_3$ requires a maximum energy input of 0.35 eV, identifying it as the potential-determining step. We have performed a climbing-image nudged elastic band (CI-NEB)[56,57] calculations for the potential-determining step of the most active catalysts (Rh$_2$@BPN and Os$_2$@BPN). The results obtained from calculations, are as summarized in Fig. S11 and S12. The calculated activation barrier for the PDS was found to be nearly zero, suggesting that the reaction proceeds without a significant kinetic barrier. Therefore, the process is considered kinetically facile, and our discussion primarily focuses on its thermodynamic aspects.

Furthermore, we extensively evaluated the catalytic activity of the related SACs (Rh@BPN, OS@BPN, and Ir@BPN). Our investigation began with identifying the stable binding site for SACs on BPN, and we found that the single metal preferentially binds on the four-membered ring rather than other binding sites, which is consistent with previous findings.[58] Subsequently, for nitrate adsorption, we considered two possible configurations, in the (1-O) configuration, one oxygen atom binds to the metal, while in the (2-O) configuration, two oxygen atoms bind to the metal. Among which the (2-O) configuration

is the most favorable on SACs, as shown in Fig. S13 and Table S13. Therefore, the 2-O configuration was selected for further reaction pathway analysis. The energy profile diagrams are shown in Fig. S14, the PDS of Rh@BPN, Os@BPN, and Ir@BPN are all *NO → *NOH, with the U_L of −1.15, −1.28, and −0.98 V, respectively. It is apparent that the performance of DACs exhibits much better catalytic activity compared to their SACs catalysts and most of the reported electrocatalysts (Table S14).

As discussed earlier, the NO$_3$RR can lead to multiple byproducts, therefore it is important to investigate the reaction pathways in more detail. Consequently, we investigated the Rh$_2$@BPN, Os$_2$@BPN, and Ir$_2$@BPN catalyst's selectivity for possible N-containing byproducts, such as NO$_2$, NO, N$_2$O, and N$_2$. Fig. 7 illustrates that the production of NO$_2$ on Rh$_2$@BPN, Os$_2$@BPN and Ir$_2$@BPN, from *OH–*NO$_2$ is not energetically feasible due to a substantial energy input of 1.11, 2.16 and 1.28 eV respectively, while the hydrogenation of *OH–*NO$_2$ is thermodynamically favorable. Additionally, a large energy input of 2.25, 2.05 and 1.80 eV were required to overcome the barrier for the direct desorption of NO$_2$ from Rh$_2$@BPN, Os$_2$@BPN and Ir$_2$@BPN respectively. Then, the removal of NO from *OH–*NO intermediate demands high energy input of 3.09, 1.58, and 1.43 eV on Rh$_2$@BPN, Os$_2$@BPN and Ir$_2$@BPN respectively. Following this, the hydrogenation of *NO on Rh$_2$@BPN, Os$_2$@BPN and Ir$_2$@BPN is slightly endothermic, with free energy changes of 0.16, 0.32, and 0.29 eV, respectively. Applying a small potential enables further hydrogenation, which is much more favorable thermodynamically than the direct desorption of NO which is high, at 2.60, 2.09, and 2.33 eV, resembling those of NO$_2$. Thus, *NO will be further hydrogenated on Rh$_2$@BPN, Os$_2$@BPN and Ir$_2$@BPN. Conversely, the NO dimer (N$_2$O$_2$), produced *via* NO–NO coupling, serves as a key precursor for the generation of N$_2$O and N$_2$. After optimization, the NO dimer undergoes bond dissociation, causing N–N bond cleavage. This implies that the NO dimer is unlikely to form, therefore N$_2$O and N$_2$ byproduct formation is also infeasible. In summary, the generation of byproducts (NO$_2$, NO, N$_2$O, and N$_2$) is effectively suppressed, indicating the high NH$_3$ selectivity of Rh$_2$@BPN, Os$_2$@BPN and Ir$_2$@BPN.

3.4 Activity origin of NO$_3$RR on TM$_2$@BPN

The activity trend of NO$_3$RR can be effectively forecasted by the adsorption energy of NO$_3^-$, thus understanding its process of activation and variation in adsorption through electronic structure analysis can provide a deeper understanding of the origin of the catalytic behavior. To begin with, the charge density differential (CDD) for TM$_2$@BPN was determined as shown in Fig. S15a and S16. The charge density difference is computed and represented as,

$$\Delta\rho = \rho(NO_3\text{–}TM_2@BPN) - \rho(TM_2@BPN) - \rho(NO_3) \quad (8)$$

where $\rho(NO_3\text{–}TM_2@BPN)$, $\rho(TM_2@BPN)$, and $\rho(NO_3)$ are the charge densities of NO$_3$ adsorbed on TM$_2$@BPN, TM$_2$@BPN, and NO$_3$, respectively. The plot indicates a significant electron transfer from the transition metal atoms to the nitrate molecule. The adsorbed nitrate gains 0.80 e$^-$, and 0.74 e$^-$ from
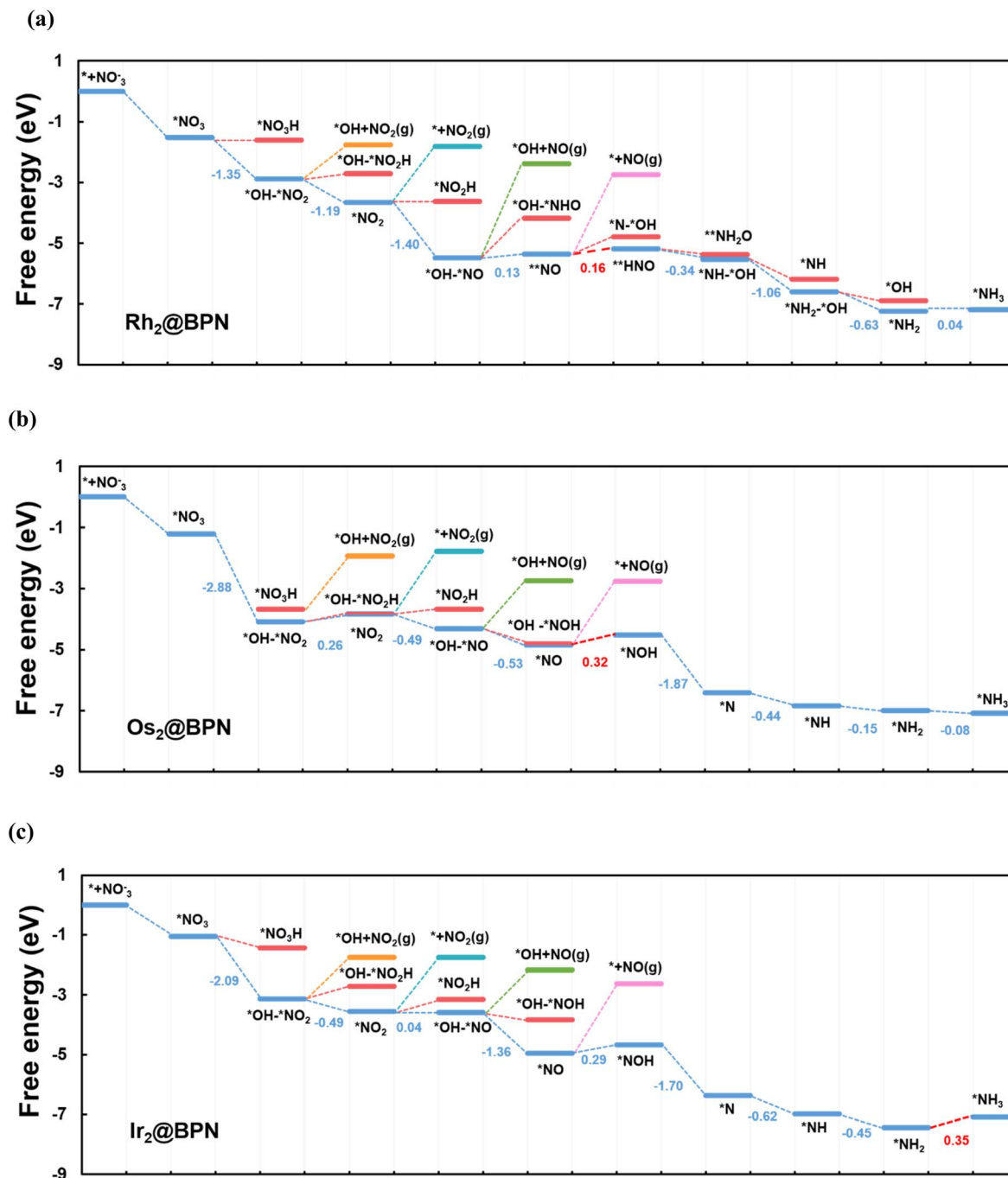
Fig. 7 (a–c) Free energy diagram for NO_3RR on $Rh_2@BPN$, $Os_2@BPN$, and $Ir_2@BPN$ catalysts respectively.

$Rh_2@BPN$, and $Os_2@BPN$ respectively. A key observation from the charge density difference analysis is the simultaneous occurrence of charge accumulation and depletion on NO_3 and transition metals. In particular, the antibonding orbitals of NO_3 are primarily filled by electrons gained from the transition metals, whereas the bonding orbitals lose some electrons to the transition metals. Consequently, the donation-back donation process allows the transition metals to efficiently activate NO_3^-.

We will now analyze the origin of $TM_2@BPN$ activity from the standpoint of orbital interactions. Fig. S15b provides

a schematic representation of the nitrate adsorption mechanism on the TM dimer substrate. In transition metal active sites, the combination of occupied and vacant d orbitals accounts for their strong binding to NO_3. The vacant d orbital of TM atoms can accept electrons from the bonding orbital of NO_3, strengthening the TM–O adsorption, whereas the occupied d-orbitals of TM atoms contribute electrons back into the empty π^* orbital of NO_3, thereby weakening the NO bond. Thus, DACs can maximize the activation potential by utilizing the d orbital of the TM dimer site through a "pull–pull" effect, or they can use

the intrinsic dual sites to increase the adjustment space.[59] Consequently, the TM dimer active site can alter the local electrical environment of the NO_3RR active site.

Fig. 8a and b presents the partial density of states (PDOS) for NO_3^- adsorbed on $Rh_2@BPN$, and $Os_2@BPN$ catalysts, while Fig. S17 displays the PDOS for the remaining systems. The PDOS analysis indicates strong π-donation from NO_3^- to the metal center, as evidenced by the overlap between the occupied NO_3^--2p orbitals and the vacant TM-d orbitals below the Fermi level. Furthermore, the small overlap above the Fermi level between the vacant NO_3^--2p orbital and the filled TM-d orbitals indicates π^*-back-donation. The d–π interaction facilitates mutual electron transfer, strengthening the interaction between NO_3^- and TM atoms and thereby stabilizing the adsorption complex. The adsorption strength is largely determined by the occupation of antibonding states. The projected crystal orbital Hamilton population (pCOHP) analysis (Fig. 8c and d) indicates that the interaction between the transition metal and nitrate exhibits predominant bonding characteristics, with a strong

bonding contribution below the Fermi level. The antibonding states are primarily located above the Fermi level, indicating that they are largely unoccupied, this implies a strong metal–adsorbate interaction.

In light of the previous explanation, transition metals' d-orbitals are important for molecular adsorption, and their energy distribution is commonly defined by the d-band center (ε_d).[60] It is widely recognized as an effective descriptor to characterize the interaction strength between small molecules and catalytic sites.[55] Therefore, we analyzed the correlation between NO_3^- free energies and the d-band center to gain insights into NO_3^- activation (Fig. 9 a). The findings indicate that ΔG_{*NO_3} and ε_d of the transition metal atoms have a linear connection. When ε_d approaches the Fermi level, the bonding states are primarily occupied while the antibonding states are largely unoccupied, resulting in greater adsorption. On the other hand, when ε_d is well below the Fermi level most of the metal's d-orbitals are filled causing the electrons to fill both bonding and antibonding orbitals formed during adsorption, causing weaker
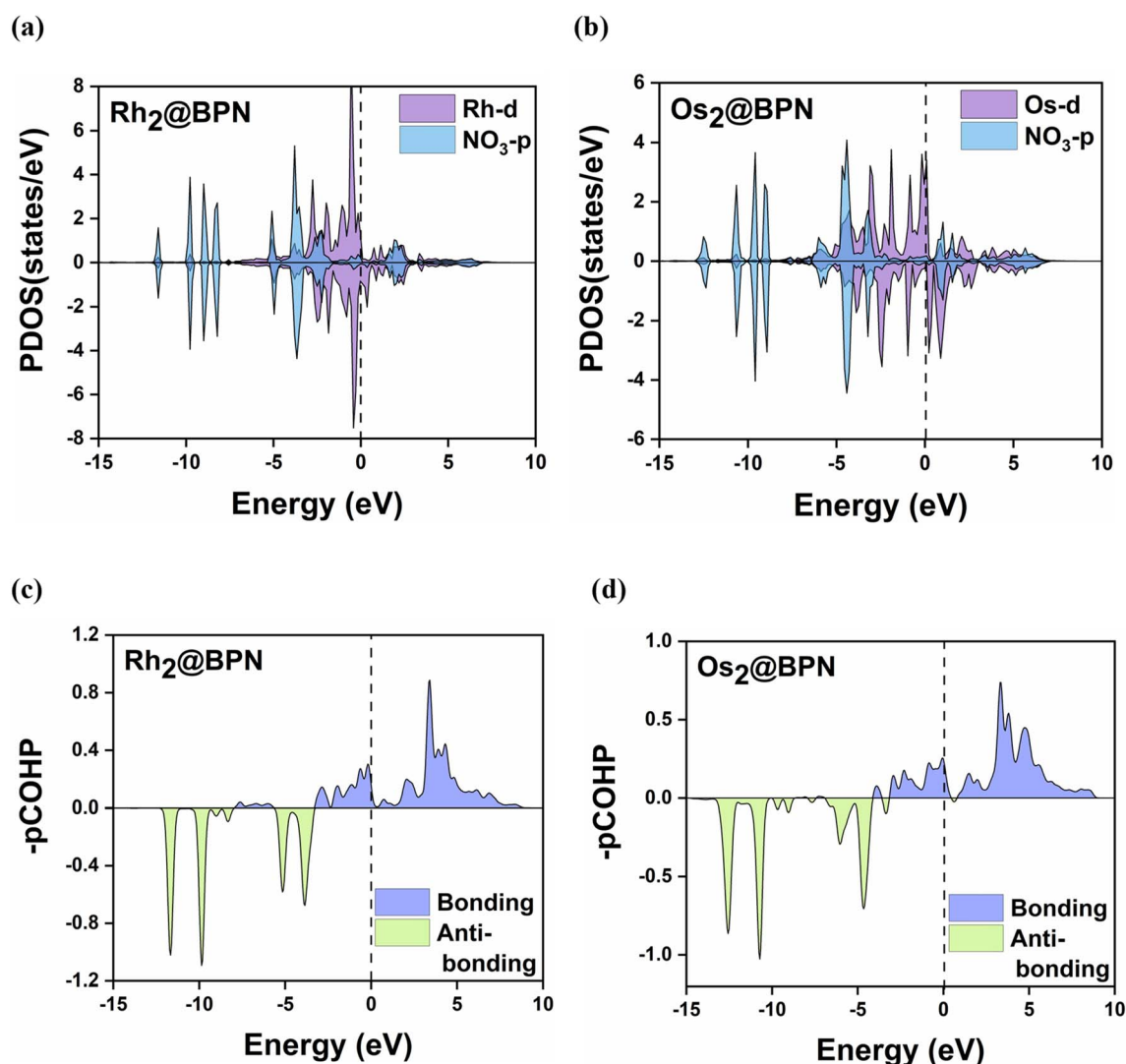

Fig. 8 (a–d) Partial density of states (PDOS) and projected crystal orbital Hamilton population (pCOHP) on the molecular orbital of NO_3 and the d orbital of metal atoms on $Rh_2@BPN$ and $Os_2@BPN$ catalyst after NO_3 adsorption.
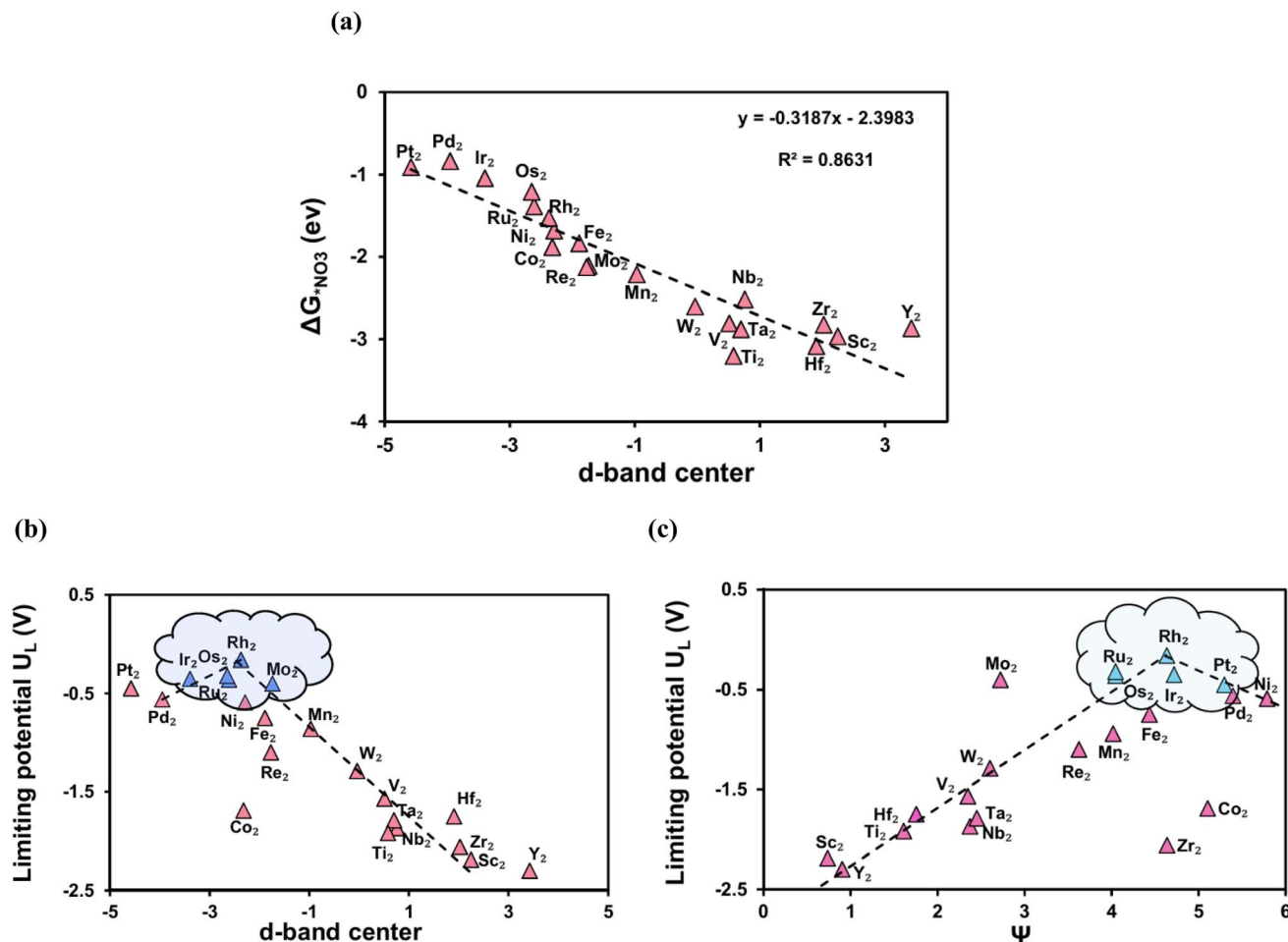
(a)

(b)

(c)

Fig. 9 (a) The liner scaling relationship between the Gibbs free energy NO_3 (ΔG_{*NO_3}) and d-band center. (b) The correlation between the limiting potential (U_L) and d-band center. (c) The correlation between the limiting potential (U_L) and descriptor ψ.

adsorption. As a result, Pt with the highest d band center (-4.58 eV), has the lowest adsorption energy (-0.91 eV). Conversely, the metal with the highest adsorption energy Ti (-3.20 eV), has the lowest d-band center (0.57 eV). Rh₂@BPN, and Os₂@BPN with optimal d-band centers of -2.37 and -2.64 eV respectively, exhibit moderate NO_3^- adsorption energies, which facilitate efficient NO₃RR. Fig. 9b shows a plot of ε_d vs. U_L for TM₂@BPN, with Rh₂@BPN at the top of the volcano, indicating superior catalytic performance. The volcano plot highlights that the excellent NO₃RR performance of DACs results from the optimal positioning of the d-band center. Additionally, we compared the d band center of SACs and DACs in order to examine the mechanism of the synergistic effect between the TM dimer site; the results are provided in Table S15. In the case of Rh@BPN, the d-band center is located at -3.26 eV, which resulted in weak nitrate adsorption (-0.96 eV). However, introducing a second Rh atom (Rh₂@BPN) shifts the d-band center closer to the Fermi level, which enhances the adsorption strength. This d-band shift significantly affects the adsorption energies of the reaction intermediates, thereby altering the energy barrier of the potential determining step.

As we have discussed earlier, the d-band is crucial for controlling catalytic activity since its occupancy affects the strength of intermediate adsorption, which in turn regulates the overall efficacy of the reaction. The quantity of d-orbital electrons (N_d), influence the adsorption strength, more d-electrons lower the d-band center, there by weakening the adsorbate binding, whereas less d-electrons enhance it, strengthening adsorption. However, N_d alone cannot explain the activity trend, this effect is further modulated by electronegativity (E_{TM}), which controls charge transfer between the transition metal and its adjacent atoms (C, N, O, or H), thereby regulating the binding of chemical intermediates. To describe the relationships between these two parameters (N_d and E_{TM}), a descriptor ψ was introduced.[61,62] Which is represented as,

$$\psi = \frac{N_d}{\sqrt{E_{TM}}} \tag{9}$$

Higher ψ generally means weaker binding to intermediates due to more filled d-orbitals leading to stronger antibonding state occupation. Fig. 9c shows a plot of ψ against U_L for TM₂@BPN, with Rh₂@BPN at the peak of the volcano plot which corresponds to the activity results. This suggests that ψ shows a strong linear correlation with adsorption energies and catalytic activity, providing a predictive tool for designing

catalysts TM$_2$@BPN screening of NO$_3$RR catalysts. Using a catalyst's easily available intrinsic nature as a descriptor to forecasting its catalytic activity provides a cost-effective and practical technique, that avoids the need for costly DFT calculations and experimental experiments.

To enable a deeper understanding of reaction pathways and electron transfer mechanisms, the gradual change of charge throughout the reaction pathway of TM$_2$@BPN for NO$_3$RR was investigated based on Bader charge analysis. Each intermediate is subdivided into three moieties (Fig. 10a), moiety 1 corresponds to (BPN support), moiety 2 is the (TM$_2$C$_4$) catalytic site and moiety 3 denotes the adsorbed intermediates involved in the reaction pathway. Fig. 10b, c and S18 display the charge variation on Rh$_2$@BPN, Os$_2$@BPN and Ir$_2$@BPN. Throughout the NO$_3$RR process, all three moieties exhibit variation in charge. During the first step, the NO$_3^-$ molecule receives 0.74 e$^-$, 0.80 e$^-$, and 0.69 e$^-$ from moiety 2 and moiety 1 on Rh$_2$@BPN, Os$_2$@BPN, and Ir$_2$@BPN respectively. The moiety 2 consistently donates electrons to the intermediates, which is important for improving the adsorption of intermediates. The final increase in moiety 3's charge signifies NH$_3$ desorption proceeds without difficulty. Thus, Rh$_2$@BPN, Os$_2$@BPN, and Ir$_2$@BPN exhibit a comparable charge variation trend. As the adsorbed intermediates receive electrons, moiety 1 facilitates electron transfer between the catalytic site and the adsorbed intermediates, allowing the catalytic process to proceed continuously, moiety 2 functions as both the DAC's active site and an electron donor.

3.5 Selectivity based on limiting potential and faradaic efficiency

Another factor that hinders NO$_3$RR performance is faradaic efficiency (FE), which is strongly related to competitive HER. To
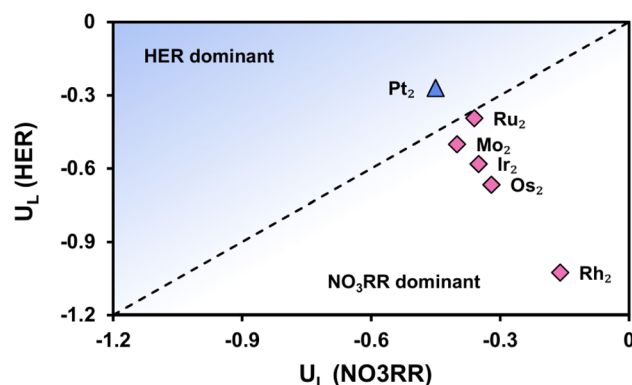

Fig. 11 Limiting potential for NO$_3$RR and HER illustrating NO$_3$RR selectivity of TM$_2$@BPN.

assess the catalytic preference of the active sites, we previously compared the $\Delta G_{*NO_3^-}$ and ΔG_{*H} values. The findings revealed that *NO$_3$ atoms are more likely to occupy the active sites than *H atoms. However, in the electrocatalytic process, U_L is the deciding element for the entire reaction. Thus, we analyze the U_L for NO$_3$RR and HER to evaluate the catalytic selectivity. Accordingly, the U_L of HER should be more negative than the U_L of NO$_3$RR. Fig. 11 illustrates the U_L of NO$_3$RR and HER, the NO$_3$RR selective is indicated by the area below the diagonal line, while the HER selective is indicated by the area above the diagonal line. Most catalysts effectively inhibit HER, with the exception of Pt. To further support this, the faradaic efficiency of NO$_3$RR was determined using the following formula:

$$FE = \left[\frac{1}{(1 + e^{-\Delta G/k_B T})}\right] \quad (10)$$

where ΔG represents the difference in free energy of the potential determining step between the HER and NO$_3$RR, k_B
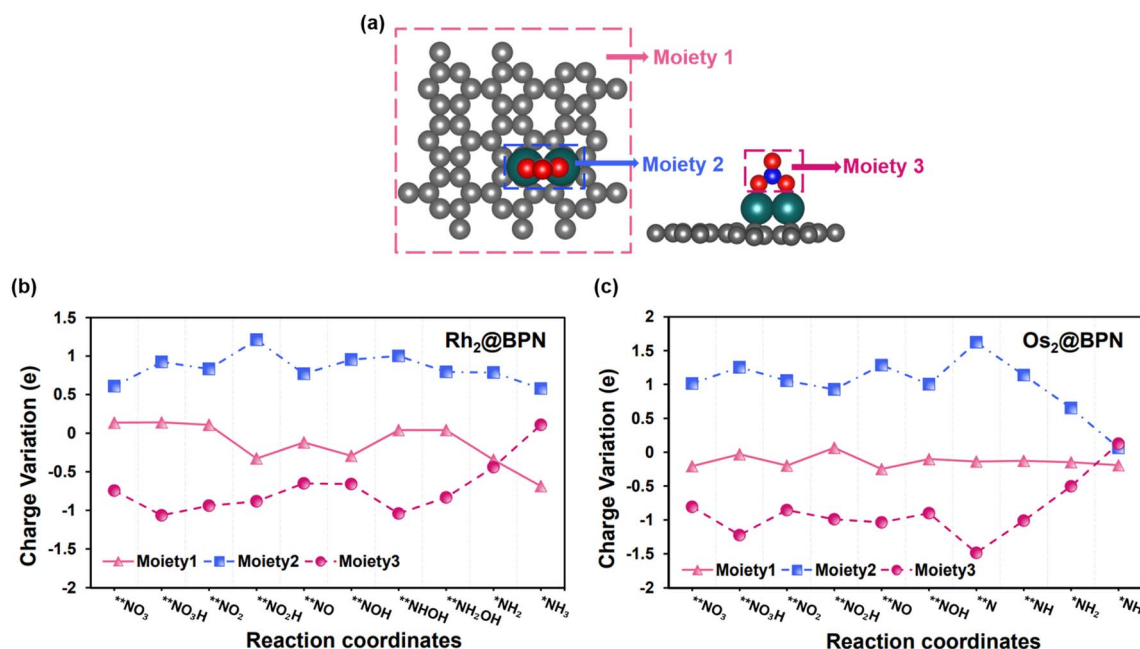

Fig. 10 (a) Three moieties of TM$_2$@BPN. (b and c) Charge variation during the process of NO$_3$RR on Rh$_2$@BPN and Os$_2$@BPN.

represents the Boltzmann constant (8.617×10^{-5} eV K^{-1}), and T represents the room temperature (298.15 K), further details are given in SI Note S3. Table S16 displays the FE value of the screened catalyst. At room temperature, the theoretical FE of NO$_3$RR on Rh$_2$@BPN can reach 100%, demonstrating its great selectivity for NO$_3$RR. Thus, Rh$_2$@BPN emerges as a highly promising candidate for NO$_3$RR considering both activity (limiting potential) and selectivity (theoretical FE).

3.6 Thermal stability of TM$_2$@BPN

Additionally, Rh$_2$@BPN, Os$_2$@BPN, and Ir$_2$@BPN were subjected to *ab initio* molecular dynamics (AIMD) simulations at 500 K for a total duration of 10 ps with a time step of 2 fs to evaluate their thermodynamic stability, as illustrated in Fig. 12 and S19. According to AIMD simulations, the structures of Rh$_2$@BPN, Os$_2$@BPN, and Ir$_2$@BPN remain stable throughout the process, without any dissociation. Furthermore, there were only slight energy variations within a narrow range. This indicates that all three materials remain stable throughout the process and are capable of withstanding high temperatures without notable structural changes.

3.7 Potential experimental synthesis

According to Fan *et al.* biphenylene (BPN) was recently synthesized by surface-assisted Ullmann coupling of 1,8-dibromobiphenylene precursors on Au (111).[35] This indicates that obtaining extended BPN sheets is experimentally feasible. A feasible technique to synthesizing double-metal anchored BPN can be developed by adapting known DAC synthesis strategies and using BPN's distinctive lattice structure. BPN is an excellent substrate for maintaining isolated dual-metal atoms because of its intrinsic periodic pores and defect-rich sites, which offer a large number of anchoring centers with a significant electron-donating capacity.[36,63] Reported approaches for DACs include high-temperature pyrolysis of metal–organic frameworks (MOFs) or zeolitic imidazolate frameworks (ZIFs), wet chemical impregnation, electrochemical deposition, and atomic layer deposition.[64,65] Using a bottom-up strategy, BPN could be impregnated with bimetallic precursors, including metal–organic complexes of Fe, Co, or Ni, and then pyrolyzed at high temperatures in an inert atmosphere to create atomically distributed dimers that are stabilized by the carbon framework. Alternatively, a sequential anchoring technique utilizing atomic layer deposition can accurately deposit two different metals onto the reactive sites of BPN, ensuring well-defined dual-atom configurations, as proven by Pt$_2$ dimers on carbon supports.[66] These methods can facilitate the controlled synthesis of double-metal anchored BPN by taking advantage of its inherent electron-rich bonding environment and high structural stability, offering a solid foundation for investigating synergistic effects in electrocatalysis.

4. Conclusion

In summary, density functional theory screening of 28 homonuclear dual-atom catalysts anchored on biphenylene (TM$_2$@BPN) establishes biphenylene as a functionally advantaged support for multistep electrocatalysis. Distinct from graphene-type lattices, BPN presents topologically diverse four-/six-/eight-membered rings and electronically anisotropic sp^2 networks, offering abundant, stabilizing anchoring motifs that promote robust dual-site fixation, favorable charge donation, and moderated adsorption energetics along the NO$_3$RR pathway. Guided by these support-induced effects, five DACs: Mo$_2$@BPN, Ru$_2$@BPN, Rh$_2$@BPN, Os$_2$@BPN, and Ir$_2$@BPN deliver low limiting potentials (−0.40 to −0.16 V) and strong ammonia selectivity, with Rh$_2$@BPN achieving a theoretical faradaic efficiency of 100% while suppressing HER and N-oxide byproducts. Mechanistically, the dual-site π-donation/π-back-donation* and d-band center tuning rationalize the activity/selectivity gains over SAC analogues. Beyond identifying high-performance catalysts, this work advances generalizable design rules: (i) target moderate NO$_3^-$ adsorption (ΔG_{*NO_3} within the volcano apex window) to avoid either early-step or late-step bottlenecks; (ii) engineer d-band centers near optimal alignment to maximize bonding while limiting antibonding population; and (iii) utilize intrinsic electronic descriptors (ΔG_{*NO_3}, ε_d, and ψ) to pre-screen dual-site compositions without exhaustive pathway calculations. These principles, corroborated by AIMD-verified thermal stability on BPN, are transferable to other multi-electron electrochemical conversions that require cooperative active sites. Collectively, our findings position biphenylene-supported DACs as a rational platform for selective nitrate-to-ammonia electroreduction and, more broadly, establish structure–property–performance correlations and descriptor-based principles that can guide the rational design of next-generation catalysts for multi-electron electrochemical transformations.
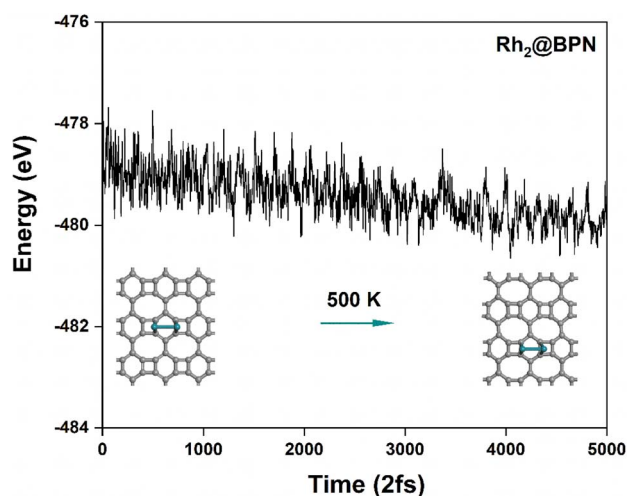
Conflicts of interest

There are no conflicts to declare.

Fig. 12 *Ab initio* molecular dynamics simulation of Rh$_2$@BPN at 500 K for a total duration of 10 ps with a time step of 2 fs.

Data availability

The data supporting the findings of this study are available within the article and its supplementary information (SI). Additional raw data are available from the corresponding author upon reasonable request.

Supplementary information: Notes 1, 2 and 3 for elementary and kinetic steps of NO_3RR, solvent effect, and faradaic efficiency, four possible binding configurations of TM dimer on BPN (Fig. S1), three possible adsorption configurations of NO_3^- on TM2@BPN (Fig. S2), DFT-optimized configurations of intermediates associated with free energy diagram of Rh_2@BPN, Os_2@BPN and Ir_2@BPN respectively (Fig. S3), free energy diagram for NO_3RR on Mo_2@BPN, Ru_2@BPN and Pt_2@BPN catalysts respectively, ($U_L > -0.5$ V) (Fig. S4), free energy diagram for NO_3RR on Sc_2@BPN, Ti_2@BPN and V_2@BPN catalysts respectively (Fig. S5), free energy diagram for NO_3RR on Mn_2@BPN, Fe_2@BPN and Co_2@BPN catalysts respectively (Fig. S6), free energy diagram for NO_3RR on Ni_2@BPN, Y_2@BPN and Zr_2@BPN catalysts respectively (Fig. S7), free energy diagram for NO_3RR on Nb_2@BPN, Pd_2@BPN and Hf_2@BPN catalysts respectively (Fig. S8), free energy diagram for NO_3RR on Ta_2@BPN, W_2@BPN and Re_2@BPN catalysts respectively (Fig. S9), three possible adsorption configurations of NO on TM2@BPN (Fig. S10), nudged elastic band calculation results for $*NO + (H_3O^+ + e^-) \rightarrow *NOH + H_2O$ on Rh_2@BPN (Fig. S11), nudged elastic band calculation results for $*NO + (H_3O^+ + e^-) \rightarrow *NOH + H_2O$ (Fig. S12), two possible adsorption configurations of NO_3^- on TM@BPN (Fig. S13), free energy diagram for NO_3RR on Rh@BPN, Os@BPN and Ir@BPN SACs catalysts respectively (Fig. S14), (a) charge density differences of nitrate adsorbed on Rh_2@BPN, and Os_2@BPN the isosurface value is 0.001 e/Å^3. (b) Schematic representation of the nitrate adsorption mechanism on the TM dimer (Fig. S15), charge density differences of nitrate adsorbed on Mo_2@BPN, Ru_2@BPN, Ir_2@BPN and Pt_2@BPN, the isosurface value is 0.001 e/Å^3. The charge depletion and accumulation were depicted by cyan and violet respectively (Fig. S16), partial density of states (PDOS) on the molecular orbital of NO_3 and the d orbital of metal atoms on Mo_2@BPN, Ru_2@BPN, Ir_2@BPN and Pt_2@BPN catalysts after NO_3 adsorption (Fig. S17), three moieties of TM$_2$@BPN and charge variation during the process of NO_3RR on Ir_2@BPN (Fig. S18), *ab initio* molecular dynamics simulation of (a) Os_2@BPN, and (b) Ir_2@BPN was carried out at 500 K for 1 ps over a total time step of fs (Fig. S19). Zero-point energy (ΔE_{ZPE}) and entropy ($T\Delta S$) at room temperature of gaseous molecules from the NIST database (Table S1), the computed binding energy (E_b), cohesive energy (E_{coh}) and the difference between binding and cohesive (E_b–E_{coh}) of TM dimers in TM$_2$@BPN (Table S2), electronic and structural properties of TM$_2$@BPN, including transition metal (TM) dimer bond length (d_{M-M}), charge transfer (CT) from TM dimer to substrate, and d band center (ε_d) (Table S3), calculated adsorption free energy ΔG_{*NO_3} (eV) on TM$_2$@BPN, *via* (η^1-O-1), (η^2-O-1) and (η^2-O-2) configuration (Table S4), transition metal to oxygen bond distance for the stable NO_3^- adsorbed

configuration (η^2-O-2) on TM$_2$@BPN (Table S5), calculated Gibbs free energy of *H (ΔG_{*H}) adsorption on TM$_2$@BPN (Table S6), calculated charge transfer (CT) from TM dimer to NO_3^-, on TM$_2$@BPN (Table S7), the Computed limiting potential (U_L) and potential determining step (PDS) of TM$_2$@BPN for NO_3RR (Table S8), the calculated Zero-point energy (ΔE_{ZPE}) and entropic contributions ($T\Delta S$) at room temperature (298.15 K) to the Gibbs free energies of each elementary step for Rh_2@BPN. The unit is eV (Table S9), the calculated Zero-point energy (ΔE_{ZPE}) and entropic contributions ($T\Delta S$) at room temperature (298.15 K) to the Gibbs free energies of each elementary step for Os_2@BPN. The unit is eV (Table S10), the calculated Zero-point energy (ΔE_{ZPE}) and entropic contributions ($T\Delta S$) at room temperature (298.15 K) to the Gibbs free energies of each elementary step for Ir_2@BPN. The unit is eV (Table S11), calculated adsorption free energy ΔG_{*NO} (eV) on TM$_2$@BPN, *via* *NO end, *ON end, and **NO side configurations (Table S12), calculated adsorption free energy ΔG_{*NO_3} (eV) on TM@BPN, *via* 1-O, and 2-O configuration (Table S13), the comparison of catalytic performance (reflected by limiting potential, U_L) for Nitrate reduction reaction on various electrocatalysts (Table S14), calculated d-band center (ε_d) of TM@BPN (Table S15), calculated limiting potential of HER and NO_3RR and faradaic efficiency (FE) values for TM$_2$@BPN (Table S16), comparison of nitrate reduction reaction pathways on the Rh_2@BPN by using DFT-D3 and DFT-Sol method (Table S17), comparison of nitrate reduction reaction pathways on the Os_2@BPN by using DFT-D3 and DFT-Sol method (Table S18). See DOI: **https://doi.org/10.1039/d5ta07089a**.

Acknowledgements

References

1 D. E. Canfield, A. N. Glazer and P. G. Falkowski, *Science*, 2010, **330**, 192–196.

2 K. R. Burow, B. T. Nolan, M. G. Rupert and N. M. Dubrovsky, *Environ. Sci. Technol.*, 2010, **44**, 4988–4997.

3 N. Gruber and J. N. Galloway, *Nature*, 2008, **451**, 293–296.

4 H. Niu, Z. Zhang, X. Wang, X. Wan, C. Shao and Y. Guo, *Adv. Funct. Mater.*, 2021, **31**, 2008533.

5 Q. Zhang, B. Liu, L. Yu, Y. Bei and B. Tang, *ChemCatChem*, 2020, **12**, 334–341.

6 Y. Wang, Y. Yu, R. Jia, C. Zhang and B. Zhang, *Natl. Sci. Rev.*, 2019, **6**, 730–738.

7 Y. Wang, A. Xu, Z. Wang, L. Huang, J. Li, F. Li, J. Wicks, M. Luo, D.-H. Nam, C.-S. Tan, Y. Ding, J. Wu, Y. Lum,

C.-T. Dinh, D. Sinton, G. Zheng and E. H. Sargent, *J. Am. Chem. Soc.*, 2020, **142**, 5702–5708.

8 J. G. Chen, R. M. Crooks, L. C. Seefeldt, K. L. Bren, R. M. Bullock, M. Y. Darensbourg, P. L. Holland, B. Hoffman, M. J. Janik, A. K. Jones, M. G. Kanatzidis, P. King, K. M. Lancaster, S. V. Lymar, P. Pfromm, W. F. Schneider and R. R. Schrock, *Science*, 2018, **360**, eaar6611.

9 H. Jiang, G.-F. Chen, O. Savateev, J. Xue, L.-X. Ding, Z. Liang, M. Antonietti and H. Wang, *Angew. Chem., Int. Ed.*, 2023, **62**, e202218717.

10 W. He, J. Zhang, S. Dieckhöfer, S. Varhade, A. C. Brix, A. Lielpetere, S. Seisel, J. R. C. Junqueira and W. Schuhmann, *Nat. Commun.*, 2022, **13**, 1129.

11 V. Rosca, M. Duca, M. T. de Groot and M. T. M. Koper, *Chem. Rev.*, 2009, **109**, 2209–2244.

12 X. Fu, X. Zhao, X. Hu, K. He, Y. Yu, T. Li, Q. Tu, X. Qian, Q. Yue, M. R. Wasielewski and Y. Kang, *Appl. Mater. Today*, 2020, **19**, 100620.

13 S. Chen, S. Perathoner, C. Ampelli, C. Mebrahtu, D. Su and G. Centi, *Angew. Chem., Int. Ed.*, 2017, **56**, 2699–2703.

14 J. M. Walls, J. S. Sagu and K. G. Upul Wijayantha, *RSC Adv.*, 2019, **9**, 6387–6394.

15 M. Duca, M. C. Figueiredo, V. Climent, P. Rodriguez, J. M. Feliu and M. T. M. Koper, *J. Am. Chem. Soc.*, 2011, **133**, 10928–10939.

16 J.-X. Liu, D. Richards, N. Singh and B. R. Goldsmith, *ACS Catal.*, 2019, **9**, 7052–7064.

17 J. Long, S. Chen, Y. Zhang, C. Guo, X. Fu, D. Deng and J. Xiao, *Angew. Chem., Int. Ed.*, 2020, **59**, 9711–9718.

18 F. Dong, M. Wu, Z. Chen, X. Liu, G. Zhang, J. Qiao and S. Sun, *Nano-Micro Lett.*, 2021, **14**, 36.

19 Y. Wang, J. Mao, X. Meng, L. Yu, D. Deng and X. Bao, *Chem. Rev.*, 2019, **119**, 1806–1854.

20 B. Singh, V. Sharma, R. P. Gaikwad, P. Fornasiero, R. Zbořil and M. B. Gawande, *Small*, 2021, **17**, 2006473.

21 H. Fei, J. Dong, Y. Feng, C. S. Allen, C. Wan, B. Volosskiy, M. Li, Z. Zhao, Y. Wang, H. Sun, P. An, W. Chen, Z. Guo, C. Lee, D. Chen, I. Shakir, M. Liu, T. Hu, Y. Li, A. I. Kirkland, X. Duan and Y. Huang, *Nat. Catal.*, 2018, **1**, 63–72.

22 Y. Wang, Y. Liu, W. Liu, J. Wu, Q. Li, Q. Feng, Z. Chen, X. Xiong, D. Wang and Y. Lei, *Energy Environ. Sci.*, 2020, **13**, 4609–4624.

23 D. K. D. Chittibabu, N. Sathishkumar, S.-Y. Wu and H.-T. Chen, *ACS Appl. Energy Mater.*, 2023, **6**, 6636–6645.

24 T. He, A. R. P. Santiago, Y. Kong, M. A. Ahsan, R. Luque, A. Du and H. Pan, *Small*, 2022, **18**, 2106091.

25 S. Zhang, W. Zhang, J. Qian, S.-z. Huang, Q. Chen, E.-y. Ming, Q. Sun and Z. Tong, Research Progress of Magnesium and Its Alloy in Petroleum Field, in *Proceedings of the International Field Exploration and Development Conference 2022, IFEDC 2022*, ed. J. Lin, Springer Series in Geomechanics and Geoengineering, Springer, Singapore, 2023, pp. 3634–3644.

26 Y. Wang, H. Yin, F. Dong, X. Zhao, Y. Qu, L. Wang, Y. Peng, D. Wang, W. Fang and J. Li, *Small*, 2023, **19**, 2207695.

27 P. Lv, D. Wu, B. He, X. Li, R. Zhu, G. Tang, Z. Lu, D. Ma and Y. Jia, *J. Mater. Chem. A*, 2022, **10**, 9707–9716.

28 F. Rehman, S. Kwon, C. B. Musgrave, M. Tamtaji, W. A. Goddard and Z. Luo, *Nano Energy*, 2022, **103**, 107866.

29 T. Zhao, K. Chen, X. Xu, X. Li, X. Zhao, Q. Cai, K. Chu and J. Zhao, *Appl. Catal., B*, 2023, **339**, 123156.

30 S. Zhang, J. Wu, M. Zheng, X. Jin, Z. Shen, Z. Li, Y. Wang, Q. Wang, X. Wang, H. Wei, J. Zhang, P. Wang, S. Zhang, L. Yu, L. Dong, Q. Zhu, H. Zhang and J. Lu, *Nat. Commun.*, 2023, **14**, 3634.

31 Z. Shu, H. Chen, X. Liu, H. Jia, H. Yan and Y. Cai, *Adv. Funct. Mater.*, 2023, **33**, 2301493.

32 M. M. Islam, S. M. Abu Nayem, S. S. Shah, M. Z. Islam, M. A. Aziz and A. J. Saleh Ahammad, *Chem. Rec.*, 2025, **25**, e202400206.

33 B. Mohanty, B. K. Jena and S. Basu, *ACS Omega*, 2020, **5**, 1287–1295.

34 J. Cho, A. Medina, I. Saih, J. Il Choi, M. Drexler, W. A. Goddard Iii, F. M. Alamgir and S. S. Jang, *Angew. Chem., Int. Ed.*, 2024, **63**, e202320268.

35 Q. Fan, L. Yan, M. W. Tripp, O. Krejčí, S. Dimosthenous, S. R. Kachel, M. Chen, A. S. Foster, U. Koert, P. Liljeroth and J. M. Gottfried, *Science*, 2021, **372**, 852–856.

36 T. Han, Y. Liu, X. Lv and F. Li, *Phys. Chem. Chem. Phys.*, 2022, **24**, 10712–10716.

37 Y. Luo, C. Ren, Y. Xu, J. Yu, S. Wang and M. Sun, *Sci. Rep.*, 2021, **11**, 19008.

38 J. Hao, Z. Zhao, C. Chen, C. Zhang, L. Li, S. Gao, B. Jia and P. Lu, *Sustainable Energy Fuels*, 2022, **6**, 3446–3452.

39 T. Liu, Y. Jing and Y. Li, *J. Phys. Chem. Lett.*, 2021, **12**, 12230–12234.

40 N. Xing, Z. Liu, Z. Wang, Y. Gao, Q. Li and H. Wang, *Phys. Chem. Chem. Phys.*, 2022, **24**, 27474–27482.

41 K. Pandiyan, D. K. Dhanthala Chittibabu and H.-T. Chen, *ACS Appl. Energy Mater.*, 2024, **7**, 10758–10769.

42 T.-T. Wang, Y. Meng, H.-C. Huang, L. Zhang and S.-B. Cheng, *Phys. Chem. Chem. Phys.*, 2025, **27**, 291–300.

43 G. Sun, J. Kürti, P. Rajczy, M. Kertesz, J. Hafner and G. Kresse, *J. Mol. Struct.:THEOCHEM*, 2003, **624**, 37–45.

44 P. E. Blöchl, *Phys. Rev. B:Condens. Matter Mater. Phys.*, 1994, **50**, 17953–17979.

45 J. P. Perdew, K. Burke and M. Ernzerhof, *Phys. Rev. Lett.*, 1996, **77**, 3865–3868.

46 S. Grimme, J. Antony, S. Ehrlich and H. Krieg, *J. Chem. Phys.*, 2010, **132**, 154104.

47 H. J. Monkhorst and J. D. Pack, *Phys. Rev. B*, 1976, **13**, 5188–5192.

48 A. Togo and I. Tanaka, *Scr. Mater.*, 2015, **108**, 1–5.

49 G. Henkelman, A. Arnaldsson and H. Jónsson, *Comput. Mater. Sci.*, 2006, **36**, 354–360.

50 V. L. Deringer, A. L. Tchougréeff and R. Dronskowski, *J. Phys. Chem. A*, 2011, **115**, 5461–5466.

51 J. K. Nørskov, J. Rossmeisl, A. Logadottir, L. Lindqvist, J. R. Kitchin, T. Bligaard and H. Jónsson, *J. Phys. Chem. B*, 2004, **108**, 17886–17892.

52 J.-C. Chen, H. Cao, J.-W. Chen, S.-J. Qian, G.-J. Xia, Y.-G. Wang and J. Li, *J. Phys. Chem. C*, 2021, **125**, 19821–19830.

53 Z. Wang, Z. Yin, Y. Gao, H. Wang, J. Gao and J. Zhao, *J. Mater. Chem. A*, 2024, **12**, 2748–2759.

54 G. Zhang, X. Li, K. Chen, Y. Guo, D. Ma and K. Chu, *Angew. Chem., Int. Ed.*, 2023, **62**, e202300054.

55 S. Jiao, X. Fu and H. Huang, *Adv. Funct. Mater.*, 2022, **32**, 2107651.

56 G. Henkelman, B. P. Uberuaga and H. Jónsson, *J. Chem. Phys.*, 2000, **113**, 9901–9904.

57 K. Chan and J. K. Nørskov, *J. Phys. Chem. Lett.*, 2015, **6**, 2663–2668.

58 D. K. D. Chittibabu and H.-T. Chen, *Electrochim. Acta*, 2024, **497**, 144578.

59 L. Yang, S. Feng and W. Zhu, *J. Hazard. Mater.*, 2023, **441**, 129972.

60 L. Yang and W. Zhu, *Diamond Relat. Mater.*, 2022, **128**, 109249.

61 H. Xu, D. Cheng, D. Cao and X. C. Zeng, *Nat. Catal.*, 2018, **1**, 339–348.

62 H. Niu, X. Wang, C. Shao, Z. Zhang and Y. Guo, *ACS Sustain. Chem. Eng.*, 2020, **8**, 13749–13758.

63 V. Kumar, S. Pratap and B. Chakraborty, *J. Phys.: Condens. Matter*, 2025, **37**, 113006.

64 D. Wu, B. He, Y. Wang, P. Lv, D. Ma and Y. Jia, *J. Phys. D: Appl. Phys.*, 2022, **55**, 203001.

65 K. Liu, J. Li, Y. Liu, M. Wang and H. Cui, *J. Energy Chem.*, 2023, **79**, 515–534.

66 H. Yan, Y. Lin, H. Wu, W. Zhang, Z. Sun, H. Cheng, W. Liu, C. Wang, J. Li, X. Huang, T. Yao, J. Yang, S. Wei and J. Lu, *Nat. Commun.*, 2017, **8**, 1070.